



Self-assembled lead-free double perovskite-MXene heterostructure with efficient charge separation for photocatalytic CO₂ reduction

Zhipeng Zhang ^{a,b,1}, Bingzhe Wang ^{a,1}, Hai-Bing Zhao ^{c,1}, Jin-Feng Liao ^a, Zi-Chun Zhou ^c, Tanghao Liu ^a, Bingchen He ^a, Qi Wei ^a, Shi Chen ^a, Hong-Yan Chen ^c, Dai-Bin Kuang ^{c,*}, Ying Li ^{b,*}, Guichuan Xing ^{a,*}

^a Joint Key Laboratory of the Ministry of Education, Institute of Applied Physics and Materials Engineering, University of Macau, Avenida da Universidade, Taipa, Macau 999078, China

^b International Collaborative Laboratory of 2D materials for Optoelectronic Science & Technology (ICL-2D MOST), Shenzhen University, Shenzhen 518060, China

^c MOE Key Laboratory of Bioinorganic and Synthetic Chemistry, Lehn Institute of Functional Materials, School of Chemistry, Sun Yat-sen University, Guangzhou 510275, China



ARTICLE INFO

ABSTRACT

Keywords:

Double perovskite nanocrystals
MXene nanosheets
Heterostructures
Charge transfer
Photocatalysis

Lead-free double perovskites with superior stability have been considered as promising non-toxic substitutes to their lead-contained counterparts in photocatalysis. However, the severe charge recombination greatly restricts their potential as high-performance photocatalysts. Herein, for the first time, we present a self-assembled heterostructure of lead-free double perovskite Cs₂AgBiBr₆ nanocrystals (NCs) on the surface of MXene nanosheets via mutual electrostatic attraction. The presence of MXene nanosheets effectively promotes the formation of free charge carriers in Cs₂AgBiBr₆ NCs via reducing the exciton binding energy. Additionally, the ultrafast photo-generated electron transfer from Cs₂AgBiBr₆ to MXene with a timescale of 1.1 ps largely prolongs the charge carrier lifetime by two times. As a result of the efficient charge separation and electron extraction, the Cs₂AgBiBr₆/MXene heterostructures achieve a high photoelectron consumption yield of 50.6 μmol g⁻¹ h⁻¹ for photocatalytic CO₂ reduction, which surpasses most previously reported lead-free perovskite-based catalysts.

1. Introduction

Lead halide perovskite nanocrystals (NCs) prepared with facile solution methods have presented phenomenal performances in optoelectronics due to a combination of attractive properties including broad absorption band with high extinction coefficients [1–3], high brightness [4], narrow-band emission [5,6], and tunable bandgap [7]. Very recently, perovskite NCs have emerged as new potential candidates in photocatalytic CO₂ reduction to directly convert CO₂ into value-added fuel and chemicals, which may help to tackle the energy shortage and environmental issues [8–13]. Nevertheless, the toxicity issue of lead-contained perovskite NCs greatly restrict their practical applications as high-performance photocatalysts [14–16]. To alleviate the toxicity of lead element, lead-free perovskites that substitute Pb²⁺ in the perovskite structure with non-toxic metal ions such as Sn²⁺ and Mn²⁺, have been reported [17–20]. Unfortunately, upon exposure to air,

Sn-based perovskites suffer from the rapid oxidation of Sn from +2 to +4 states [21]. Although the divalent cation Mn²⁺ is stable and can be easily doped to the Pb²⁺ site in the perovskite structure, a full substitution of Pb²⁺ is unable to achieve [19].

Recently, lead-free double perovskite A₂MM'X₆ (A = Cs; M = Ag, Na; M' = Bi, In; X = Cl, Br, I) obtained by replacing Pb²⁺ cation with one monovalent M⁺ and one trivalent M'³⁺ cation alternately has attracted intense scientific interest [22,23]. This class of compounds tend to be significantly more stable to thermal, light and moisture than their lead-contained counterparts [24]. The structural and functional diversity with outstanding stability makes double perovskites promising non-toxic candidates in optoelectronics and photocatalysis [25,26]. Among them, all inorganic double perovskite Cs₂AgBiBr₆ has demonstrated its potential in photocatalytic CO₂ reduction [27] and H₂ evolution [28,29] due to the excellent stability and a suitable bandgap of 1.8–2.2 eV [26]. However, Cs₂AgBiBr₆ suffers from a large exciton

* Corresponding authors.

E-mail addresses: kuangdb@mail.sysu.edu.cn (D.-B. Kuang), queenly@szu.edu.cn (Y. Li), gcxing@um.edu.mo (G. Xing).

¹ These authors contributed equally.

binding energy, which is unfavorable for the charge separation, thus limiting the performance in photocatalytic reactions [25,30,31]. For example, Zhou et al. demonstrated the use of $\text{Cs}_2\text{AgBiBr}_6$ NCs as photocatalyst in CO_2 reduction reaction with a moderate electron consumption of $17.5 \mu\text{mol g}^{-1} \text{ h}^{-1}$ [27]. Although recent work shows the photoactivity can be improved through a morphology engineering strategy, the result is still far from satisfactory [32].

As a novel member of 2D material family, transition metal carbides, carbonitrides and nitrides, that is known as MXene, have attracted intensive research attention [33–36]. The general formula of MXene is $M_{n+1}X_nT_x$, where M is early transition metal, X represents carbon and/or nitrogen, and T_x stands for surface groups. Benefit from their good conductivity, high electric capacity, high elastic moduli and tunable bandgap [35], MXenes have shown potential in a variety of applications, such as capacitors [37], ion batteries [38], field-effect transistors [39] and electromagnetic interference shielding [40]. However, these atomic-thin 2D nanosheets usually suffer from limited light-absorbing ability [41,42]. Thus, decorating MXene with $\text{Cs}_2\text{AgBiBr}_6$ NCs may largely improve the light absorption by taking advantage of the excellent optical properties of perovskite NCs. Besides, MXene with good electron transfer property is supposed to facilitate the charge separation and transport of $\text{Cs}_2\text{AgBiBr}_6$ NCs. Moreover, 2D MXene nanosheets with large specific surface area and rich active sites may significantly improve the performance of catalytic reaction [43,44].

In this work, lead-free double perovskite $\text{Cs}_2\text{AgBiBr}_6$ NCs were self-assembled on the surface of few-layer MXene nanosheets through a facile solution method for the first time. The microstructure, morphology, and surface chemical state of $\text{Cs}_2\text{AgBiBr}_6$ /MXene heterostructures were carefully characterized. Our systematic experimental observation reveals the presence of MXene nanosheets effectively promotes formation of free charge carriers in $\text{Cs}_2\text{AgBiBr}_6$ NCs. The efficient photoelectron transfer from $\text{Cs}_2\text{AgBiBr}_6$ to MXene leads to the formation of a long-lived charge separate state. Taking advantage of the synergistic features, the $\text{Cs}_2\text{AgBiBr}_6$ /MXene heterostructures achieve a high photoelectron consumption yield of $50.6 \mu\text{mol g}^{-1} \text{ h}^{-1}$ for photocatalytic CO_2 reduction, which is 98.4% and 148.0% higher than that of pristine $\text{Cs}_2\text{AgBiBr}_6$ and $\text{Ti}_3\text{C}_2\text{T}_x$, respectively.

2. Experimental section

2.1. Materials

Ti_3AlC_2 MAX powder (200 mesh, Forsman Technology, China), hydrofluoric acid (HF, 50 wt%, Aladdin, China), tetramethylammonium hydroxide (TMAOH, 25 wt% in water, Aladdin, China), ascorbic acid (AA, 99%, Sigma, USA), bismuth (III) bromide (BiBr_3 , 99%, Alfa, USA), silver nitrate (AgNO_3 , 99.9995%, Alfa, USA), cesium carbonate (Cs_2CO_3 , 99.9%, Sigma, USA), oleic acid (OA, 85.0%, Aladdin, China), oleyl amine (OLA, 80–90%, Aladdin, China), hydrobromic acid (HBr, 48%, Sigma, USA), 1-octadecene (ODE, 90%, Acros, USA), *N*, *N*-dimethylformamide (DMF, analytical reagent, Shanghai Chemical Reagent Co., Ltd., China), toluene (analytical reagent, Shanghai Chemical Reagent Co., Ltd., China) and ethyl acetate (99.8%, Sigma, USA) were used as received without further purification.

2.2. Preparation of few-layer $\text{Ti}_3\text{C}_2\text{T}_x$ nanosheets

The few-layer $\text{Ti}_3\text{C}_2\text{T}_x$ nanosheets were prepared with a hydrothermal assisted intercalation method. Briefly, the Ti_3AlC_2 MAX powder was firstly etched by HF to obtain the multi-layer $\text{Ti}_3\text{C}_2\text{T}_x$. To obtain few-layer $\text{Ti}_3\text{C}_2\text{T}_x$ nanosheets, 50 mg of the multi-layer $\text{Ti}_3\text{C}_2\text{T}_x$ MXene and 176 mg AA was loaded into 16 mL of 2 wt% TMAOH aqueous solution. After stirring for 20 min, this solution was transferred to a 50 mL Teflon-lined stainless-steel autoclave and heated to 140 °C for 24 h. When the autoclave was cooled down to room temperature, the product was collected and washed with deionized water for three cycles. Afterwards,

the $\text{Ti}_3\text{C}_2\text{T}_x$ solution was sonicated in ice-bath under N_2 protection for 30 min. After centrifugation at 3500 rpm for 30 min, few-layer $\text{Ti}_3\text{C}_2\text{T}_x$ MXene nanosheets was obtained by discarding the precipitate. The MXene solution was then centrifuged at 12,000 rpm and washed with DMF for three times to form a concentrated suspension for further use.

2.3. Synthesis of Cs-oleate

0.204 g Cs_2CO_3 , 10 mL ODE and 0.6 mL OA were loaded into a 25 mL 3-neck flask. Then the mixture was heated to 120 °C for 1 h to remove residual gases and water. After that, this solution was heated to 150 °C under N_2 protection for 10 min.

2.4. Synthesis of $\text{Cs}_2\text{AgBiBr}_6$ NCs

Typically, 45 mg BiBr_3 , 17 mg AgNO_3 , 4 mL ODE and 0.1 mL HBr were loaded into a 25 mL 3-necked flask followed by injection of 1 mL OA and 1 mL OLA. Then this solution was dried and degassed at 120 °C for 1 h. After that, this solution was heated to 200 °C under N_2 protection. Subsequently, 0.8 mL Cs-oleate was injected to this mixture swiftly under quick stirring. After 5 s, the reaction mixture was put into an ice-water bath to cool down to room temperature. The reaction mixture was then centrifuged at 10,000 rpm for 10 min to leave a yellow precipitate. After the precipitate was washed with a mixed solution ($V_{\text{toluene}}: V_{\text{ethyl acetate}} = 2: 1$) for three times, the NCs were redispersed in toluene and centrifuged at 1000 rpm for 10 min. The $\text{Cs}_2\text{AgBiBr}_6$ NCs were then obtained by discarding the bottom precipitates.

2.5. Preparation of $\text{Cs}_2\text{AgBiBr}_6/\text{Ti}_3\text{C}_2\text{T}_x$ heterostructures

For the fabrication of $\text{Cs}_2\text{AgBiBr}_6/\text{Ti}_3\text{C}_2\text{T}_x$ heterostructures, 50 μL of the afore-mentioned few-layer $\text{Ti}_3\text{C}_2\text{T}_x$ DMF suspension (~3 mg/mL) was slowly dropped into 3 mL toluene under ultrasonication to form a homogeneous suspension. To this suspension, 100 μL of $\text{Cs}_2\text{AgBiBr}_6$ toluene solution (~5 mg/mL) was added. Then the mixture was subjected to ice-bath sonication for 10 min under N_2 atmosphere. After centrifugation at 10,000 rpm for 10 min, the precipitates were collected and washed three times with toluene for further characterizations.

2.6. Characterizations

The morphological and structural characterizations of the products were examined by scanning electron microscopy (SEM, Zeiss SIGMA, USA), transmission electron microscopy (TEM, Talos F200S, USA), high resolution transmission electron microscopy (HRTEM, Talos F200S, USA), high-angle annular dark-field scanning transmission electron microscopy (HAADF-STEM, Talos F200S, USA), atomic force microscopy (AFM, Bruker Dimension ICON, Germany), Kelvin probe force microscopy (KPFM, Bruker Dimension ICON, Germany), ultraviolet photoelectron spectra (UPS, Thermo Fischer ESCALAB 250Xi, USA) and X-ray diffraction (XRD, SmartLab Rigaku, Japan, $\text{Cu K}\alpha$ radiation, $\lambda = 1.54056 \text{ \AA}$). The Zeta potential of samples was determined using a Zetasizer equipment (Nano ZS90, Malvern Instruments, UK). UV-vis absorption spectra of the samples were performed on a UV-vis spectrophotometer (V-770, Jasco, Japan). The room-temperature and low-temperature photoluminescence (PL) spectra were recorded by a fluorescence spectrophotometer (SP-2300, Princeton Instruments, USA). The femtosecond transient absorption (TA) spectra of different samples were taken using the Ultrafast System HELIOS TA spectrometer. The Coherent Legend regenerative amplifier (150 fs, 1 kHz, 800 nm) seeded by a Coherent Vitesse oscillator (100 fs, 80 MHz) was used as the laser source. 370 nm pump light was generated from a Light Conversion TOPAS-C optical parametric amplifier. The Brunauer-Emmett-Teller (BET) surface area was measured by nitrogen adsorption-desorption isotherms at 77 K with a JW-BK200C system (JWGB SCI & TECH, China). All samples were degassed at 150 °C for 10 h prior to

measurements. The BET-specific surface area was calculated using the single point BET method in the linear relative pressure range of 0.05–0.25. CO₂ adsorption isotherms were measured at 298 K using an ASAP 3020 carbon dioxide adsorption apparatus (Micromeritics, USA).

2.7. Photoelectrochemical measurements

Photoelectrochemical measurements were performed in a three-electrode electrochemical quartz glass cell. 0.1 M ammonium hexafluorophosphate in dichloromethane was used as the electrolyte. The pristine Cs₂AgBiBr₆ and Cs₂AgBiBr₆/Ti₃C₂T_x thin films for I-T curve measurement were fabricated through a centrifugally cast process. First, the ITO glasses were sliced into the size of approximately 1.5 cm × 1.5 cm and sonicated in deionized water, alcohol, and acetone for 10 min subsequently. Then, the ITO glass was placed inside a 10 mL centrifugation tube, with the conduction side facing down before the centrifugally cast process. Cs₂AgBiBr₆ and Cs₂AgBiBr₆/Ti₃C₂T_x suspension were added into the centrifugation tube and then centrifuged at 10,000 rpm for 30 s to deposit Cs₂AgBiBr₆ and Cs₂AgBiBr₆/Ti₃C₂T_x onto the FTO glasses. The thickness of the films applied to the photoelectrochemical characterization and I-T curve measurement is about 3.8 μm according to surface profile measurement. The bias used in the I-T curve measurement was 0.1 V. Ag/AgCl (saturated KCl) and Pt mesh were used as the reference electrode and the counter electrode, respectively. The light source is a Xenon light (150 mW cm⁻², 400 nm filter, Newport LCS-100) and the light on/off was controlled by Light chopping equipment (PFS40A, Beijing Perfect Light Technology Co., Ltd.).

2.8. Photocatalytic measurements

Photocatalytic CO₂ reduction reaction was performed in a sealed quartz glass cell with 5 mg samples under high purity CO₂ and 20 μL of H₂O atmosphere. The light source is a Xenon light (150 mW cm⁻², 400 nm filter, Newport LCS-100). The products were analyzed by gas chromatography (GC9790 plus, Fuli Analytical Instrument Co., Ltd.). The electron consumption yield was calculated with the following equation:

$$Y(\text{electron}) = 2Y(\text{H}_2) + 2Y(\text{CO}) + 8Y(\text{CH}_4)$$

2.9. Apparent quantum yield (AQY) measurement

The AQY was characterized on a multi-channel photocatalytic reaction system (PCX-50B, Beijing Perfectlight, China). The monochromatic incident light was provided by a series of light-emitting diodes (LEDs). AQY at a specific wavelength was calculated by the function:

$$\text{AQY} (\%) = \frac{N_{\text{electron}}}{N_{\text{photon}}} = \frac{[2 N(\text{CO}) + 8 N(\text{CH}_4) + 2 N(\text{H}_2)]}{N_{\text{photon}}} = \frac{[2 N(\text{CO}) + 8 N(\text{CH}_4) + 2 N(\text{H}_2)]}{[I \times A \times t] / (E_{\text{photon}} \times N_A)}$$

where N(CO), N(CH₄) and N(H₂) represents the amounts of CO, CH₄ and H₂, respectively; I is the incident light intensity; A is the illumination area; E_{photon} is the average single photon energy that is calculated with the function: E_{photon} = hc/λ; N_A is Avogadro's constant.

2.10. Computational details

The spin-polarized density functional theories (DFT) were carried out by using the Vienna Ab initio Simulation Package (VASP). The Perdew-Burke-Ernzerhof generalized-gradient approximation functional was used to describe the interaction between electrons. The energy cutoff was set to 400 eV. The 7-centered k-points grid was set to be 2 × 2 × 1 for all the calculations. The vacuum region was set to be 15 Å in z direction to prevent the interaction between two adjacent surfaces. The energy convergence was set to 10⁻⁵ eV. The atomic positions of the

bottom layer were fixed during the simulation.

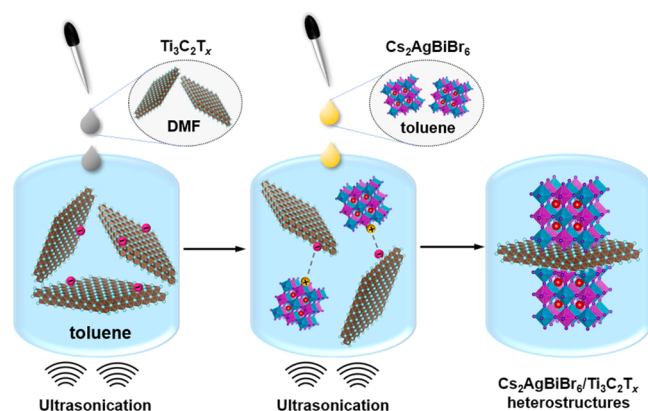
The reaction Gibbs free energy (ΔG) is defined as ΔG = ΔE + ΔE_{ZPE} - TΔS, ΔE is the reaction energy, ΔE_{ZPE} is zero-point energies, T is the temperature (298.15 K), ΔS is the difference in entropy from vibrational frequency calculations. The entropies of gas phase CO₂, H₂ and H₂O are obtained from the NIST database with the standard condition.

3. Results and discussions

3.1. Synthesis, structure and morphology of Cs₂AgBiBr₆/Ti₃C₂T_x heterostructures

As shown in **Scheme 1**, the Cs₂AgBiBr₆/MXene heterostructures were fabricated via an ultrasonication-assisted self-assembly process. Few-layer Ti₃C₂T_x nanosheets were obtained following a previously reported hydrothermal assisted intercalation approach [45] and cubic-phased Cs₂AgBiBr₆ NCs were synthesized by a hot-injection method [27] (see Fig. S1, S2 and Experimental Section for details). To realize the self-assembly of Cs₂AgBiBr₆ NCs on few-layer Ti₃C₂T_x nanosheets, both components were mixed in solution with a specific ratio. First, a certain amount of Ti₃C₂T_x nanosheets was added dropwise into toluene under ultrasonication. Subsequently, Cs₂AgBiBr₆ NCs were added and then the mixture was sonicated under the protection of N₂ atmosphere to induce the self-assembly of Cs₂AgBiBr₆ NCs on Ti₃C₂T_x nanosheets. Previous reports reveal that MXene nanosheets are abundant with surface terminations such as fluorine, oxygen, and hydroxyl groups [46,47], which are inclined to interact with surface ligands of Cs₂AgBiBr₆ NCs [47–50]. The strong electrostatic attraction between Cs₂AgBiBr₆ NCs and Ti₃C₂T_x nanosheets was verified by their zeta potential values. As shown in Fig. 1a, the Cs₂AgBiBr₆ NCs show a positive zeta potential of 86.7 mV whereas the Ti₃C₂T_x nanosheets possess a negative zeta potential of -39.0 mV. The opposite surface charges would result in strong electrostatic attraction between them, leading to the spontaneous assembly of Cs₂AgBiBr₆ NCs on Ti₃C₂T_x nanosheets and formation of a close heterointerface [43]. Moreover, the large specific surface area of 2D MXene nanosheets combined with abundant surface groups may provide more chances for Cs₂AgBiBr₆ NCs to self-assemble themselves through the Coulomb electrostatic interaction [43]. Fig. S3 shows the photographs of MXene nanosheets and Cs₂AgBiBr₆/MXene heterostructures dispersed in a mixed DMF/toluene solvent (V_{DMF}: V_{toluene} = 1: 60) during the synthesis. The MXene nanosheets exhibit a poor dispersibility. Interestingly, when Cs₂AgBiBr₆ NCs were added, the as-obtained Cs₂AgBiBr₆/MXene heterostructures were well dispersed after sonication. This further suggests that Cs₂AgBiBr₆ NCs are decorated on the surface of MXene nanosheets, which greatly improve the dispersibility of MXene nanosheets.

The crystal structures of the Cs₂AgBiBr₆/Ti₃C₂T_x heterostructures



Scheme 1. Schematic illustration of the self-assembly process of Cs₂AgBiBr₆ NCs on few-layer Ti₃C₂T_x nanosheets.

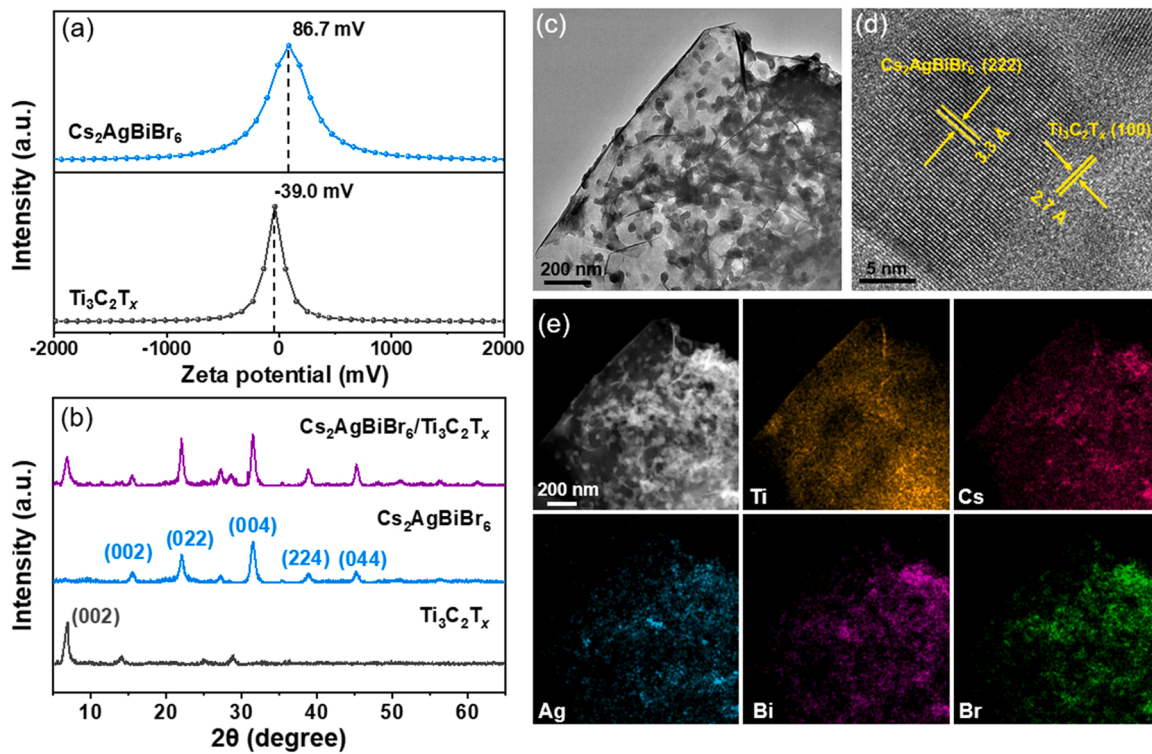


Fig. 1. (a) Zeta potentials of Cs₂AgBiBr₆ NCs and Ti₃C₂T_x nanosheets. (b) XRD patterns of Cs₂AgBiBr₆, Ti₃C₂T_x and Cs₂AgBiBr₆/Ti₃C₂T_x heterostructures. (c) TEM and (d) HRTEM images of Cs₂AgBiBr₆/Ti₃C₂T_x heterostructures. (e) HAADF-STEM image of Cs₂AgBiBr₆/Ti₃C₂T_x heterostructures and the corresponding EDS mapping images of Cs, Ag, Bi, Br and Ti elements.

were determined by X-ray diffraction (XRD) in Fig. 1b. The characteristic diffraction peaks detected at $2\theta = 15.4^\circ$, 21.9° , 31.1° , 38.3° , and 45.2° are consistent with that of cubic-phased (*Fm3m*) Cs₂AgBiBr₆ with $a = 11.48 \text{ \AA}$ [23]. Apart from the characteristic diffraction peaks of Cs₂AgBiBr₆, an additional peak at around 6.3° was detected, which can be unambiguously assigned to the (002) planes of Ti₃C₂T_x [51]. The presence of the XRD peaks for both Cs₂AgBiBr₆ and Ti₃C₂T_x indicates the successful preparation of Cs₂AgBiBr₆/Ti₃C₂T_x heterostructures. Fig. S4 shows the X-ray photoelectron spectroscopy (XPS) full spectra of pristine Ti₃C₂T_x MXene, Cs₂AgBiBr₆ NCs and Cs₂AgBiBr₆/Ti₃C₂T_x heterostructures. For pristine MXene, characteristic peaks corresponding to F 1 s, O 1 s, C 1 s, and Ti 2p were observed, which were expected for Ti₃C₂T_x terminated with O, OH, and/or F groups [52]. For the Cs₂AgBiBr₆/Ti₃C₂T_x heterostructures, additional peaks corresponding to Cs 3d, Ag 3d, Bi 4f and Br 3d binding energies were detected, consistent with the presence of Cs₂AgBiBr₆ NCs in the heterostructures. To determine the compositional ratio of Cs₂AgBiBr₆/MXene, scanning electron microscopy/energy dispersive X-ray spectrometry (SEM-EDS) was used. As shown in Fig. S5, the elements Cs, Ag, Bi, Br, Ti and C were clearly determined from the SEM-EDS spectrum. Based on the atomic ratio listed in Table S1, the molar ratio of Cs₂AgBiBr₆/Ti₃C₂T_x was estimated to be $\sim 1:1$, corresponding with a mass ratio of $\sim 6:1$.

The morphology of Cs₂AgBiBr₆/Ti₃C₂T_x heterostructures was analyzed by transmission electron microscopy (TEM). Pristine Ti₃C₂T_x nanosheets are electron-transparent with a smooth surface (Fig. S6), indicating the few-layer nature, which is consistent with AFM measurements (Fig. S1). The TEM image of Cs₂AgBiBr₆/Ti₃C₂T_x heterostructures in Fig. 1c unambiguously reveals the Cs₂AgBiBr₆ NCs are evenly adhered on the surface of Ti₃C₂T_x nanosheet. The low-magnification TEM image of Cs₂AgBiBr₆/Ti₃C₂T_x heterostructures in Fig. S7 clearly shows that most of the Cs₂AgBiBr₆ NCs are self-assembled on the surface of MXene nanosheets. It was also observed that some of the NCs turn from square to round, indicating the strong interaction between Cs₂AgBiBr₆ and Ti₃C₂T_x [9]. This phenomenon is commonly

observed in previously reported perovskite nanocomposite synthesized by solution method [53,54]. The shape change can be generally attributed to the dissolution and recrystallization behavior of perovskite NCs. During the synthesis process, the ligands encapsulated on the surface of Cs₂AgBiBr₆ NCs may drop due to ultrasonication effect and the use of a small amount of polar solvent DMF. Then some of the Cs₂AgBiBr₆ NCs would dissolve and recrystallize, leading to the shape turning from square to round after being incorporated with MXene. As such, the average size of Cs₂AgBiBr₆ NCs after being incorporated with MXene increased from 13.6 to 32.2 nm (Fig. S2d and Fig. S8). The high-resolution TEM (HRTEM) image of Cs₂AgBiBr₆/Ti₃C₂T_x heterostructures in Fig. 1d further confirms the distribution of Cs₂AgBiBr₆ NCs on Ti₃C₂T_x nanosheets. The HRTEM image displays two obvious lattice *d*-spacings of 3.3 and 2.7 Å in different directions, which can be assigned to the (222) planes of Cs₂AgBiBr₆ and (100) planes of Ti₃C₂T_x, respectively [35]. To further investigate the detailed feature of Cs₂AgBiBr₆/Ti₃C₂T_x heterostructures, the high-angle annular dark-field scanning transmission electron microscopy (HAADF-STEM) and energy-dispersive X-ray spectroscopy (EDS) were utilized. The distribution of the elements Cs, Ag, Bi, Br and Ti determined from the EDS elemental mapping in Fig. 1e reveals that Cs₂AgBiBr₆ NCs are homogeneously distributed on the Ti₃C₂T_x nanosheets, which further confirms the successful preparation of Cs₂AgBiBr₆/Ti₃C₂T_x heterostructures.

The surface chemical state of Cs₂AgBiBr₆/Ti₃C₂T_x heterostructures was investigated by XPS. As shown in Fig. S9a, the high-resolution Cs 3d spectra of Cs₂AgBiBr₆ show two narrow peaks at ~ 737.90 and 723.99 eV, which are assigned to the binding energies of Cs 3d_{5/2} and Cs 3d_{3/2}, respectively [28]. Compared with pristine Cs₂AgBiBr₆, these peaks positively shift by ~ 0.3 eV to 738.21 and 724.30 eV when they are adhered to the surface of Ti₃C₂T_x nanosheets. A similar positive shift of XPS binding energies is also found in Ag 3d, Bi 4f and Br 3d spectra (Fig. S9b-d). In contrast, the binding energies of Ti, C, O and F elements in Ti₃C₂T_x show the opposite trend as shown in Fig. S10, indicate the migration of electron density from Cs₂AgBiBr₆ to Ti₃C₂T_x through the

established heterogeneous interfaces [55–57]. However, there is no evidence suggesting the interfacial bonding formation between $\text{Cs}_2\text{AgBiBr}_6$ and $\text{Ti}_3\text{C}_2\text{T}_x$.

The surface area and CO_2 adsorption ability of $\text{Cs}_2\text{AgBiBr}_6/\text{Ti}_3\text{C}_2\text{T}_x$ heterostructures and their single components were investigated. As shown in Fig. S11, the surface area for $\text{Cs}_2\text{AgBiBr}_6$, $\text{Ti}_3\text{C}_2\text{T}_x$, and $\text{Cs}_2\text{AgBiBr}_6/\text{Ti}_3\text{C}_2\text{T}_x$ were measured to be 6.0, 94.1 and $60.2 \text{ cm}^2 \text{ g}^{-1}$, respectively. The CO_2 adsorption for $\text{Cs}_2\text{AgBiBr}_6$, $\text{Ti}_3\text{C}_2\text{T}_x$, and $\text{Cs}_2\text{AgBiBr}_6/\text{Ti}_3\text{C}_2\text{T}_x$ were 1.62, 3.46 and $10.73 \text{ cm}^2 \text{ g}^{-1}$, respectively. The surface area and CO_2 capture ability of $\text{Cs}_2\text{AgBiBr}_6/\text{Ti}_3\text{C}_2\text{T}_x$ heterostructures are significantly enhanced compared to $\text{Cs}_2\text{AgBiBr}_6$ due to the high surface area of 2D MXene nanosheets, which may provide more photocatalytic sites for CO_2 reduction.

3.2. Charge carrier dynamics in $\text{Cs}_2\text{AgBiBr}_6/\text{Ti}_3\text{C}_2\text{T}_x$ heterostructures

UV-vis absorption spectra of the $\text{Cs}_2\text{AgBiBr}_6/\text{Ti}_3\text{C}_2\text{T}_x$ heterostructures in comparison with that of pristine $\text{Cs}_2\text{AgBiBr}_6$ NCs and $\text{Ti}_3\text{C}_2\text{T}_x$ nanosheets are shown in Fig. 2a. The $\text{Cs}_2\text{AgBiBr}_6$ NCs exhibit a typical absorption spectrum featuring a sharp exciton absorption peak positioned at $\sim 435 \text{ nm}$ and an absorption onset at $\sim 520 \text{ nm}$, suggesting an indirect transition, which is consistent with previous reports [27]. Compared to $\text{Cs}_2\text{AgBiBr}_6$, the exciton band of $\text{Cs}_2\text{AgBiBr}_6/\text{Ti}_3\text{C}_2\text{T}_x$ heterostructures shows a slight redshift while an additional broad absorption feature in the UV-vis region is also observed. The latter can be attributed to the broadband absorption of $\text{Ti}_3\text{C}_2\text{T}_x$ nanosheets [45]. On the other hand, $\text{Cs}_2\text{AgBiBr}_6$ NCs show a weak and broad emission centered at $\sim 660 \text{ nm}$, which is attributed to the recombination of indirect bound excitons, similar to previous reports [23,30]. The broadband PL emission of $\text{Cs}_2\text{AgBiBr}_6$ NCs was intensively quenched when they were self-assembled on $\text{Ti}_3\text{C}_2\text{T}_x$ nanosheets (Fig. 2b). The dramatically reduced PL intensity of $\text{Cs}_2\text{AgBiBr}_6$ after hybridization with $\text{Ti}_3\text{C}_2\text{T}_x$ suggest the presence of MXene nanosheets may dramatically influence the formation of excitons [58,59]. To extract the exciton

binding energy that related to the formation of excitons, temperature-related photoluminescence was recorded. As shown in Fig. S12, the PL intensity of both pristine $\text{Cs}_2\text{AgBiBr}_6$ and $\text{Cs}_2\text{AgBiBr}_6/\text{Ti}_3\text{C}_2\text{T}_x$ heterostructures becomes weaker when temperature rises from 40 to 300 K. The integrated PL intensity was plotted as a function of temperature using the Arrhenius equation:[60,61].

$$I(T) = \frac{I_0}{1 + A \exp\left(\frac{E_b}{k_B T}\right)} \quad (1)$$

where I_0 is the intensity at 0 K, E_b represents the activation energy for exciton dissociation, and k_B is Boltzmann constant. Fig. 2c shows the integrated PL intensity versus temperature from 40 to 300 K. The activation energies are estimated to be 55 and 39 meV for pure $\text{Cs}_2\text{AgBiBr}_6$ and $\text{Cs}_2\text{AgBiBr}_6/\text{Ti}_3\text{C}_2\text{T}_x$ heterostructures, respectively. This implies that the presence of $\text{Ti}_3\text{C}_2\text{T}_x$ in the heterostructures leads to a lower exciton binding energy and promotes the formation of free carriers in $\text{Cs}_2\text{AgBiBr}_6$ NCs [62].

To further explore the charge carrier dynamics in $\text{Cs}_2\text{AgBiBr}_6/\text{Ti}_3\text{C}_2\text{T}_x$ heterostructures, transient absorption (TA) measurements have been conducted. The detailed bleaching kinetics of both samples are fitted with a multi-exponential function and shown in Table S2. Upon photo excitation, pristine $\text{Cs}_2\text{AgBiBr}_6$ NCs at different time delays with a negative photobleaching (PB) feature around 439 nm that corresponds with the exciton absorption were observed, as shown in Fig. 2d [63]. By tracing the ground state recovery kinetic of the exciton PB feature (Fig. 2f), there firstly demonstrates two fast decay processes with lifetimes around 4.2 and 151.8 ps, corresponding with the intervalley scattering processes [30,64]. As follows, a long tail with lifetime of $\sim 4.6 \text{ ns}$ is attributed to the relaxed carriers at the indirect band edge. Fig. 2e shows the TA spectra of $\text{Cs}_2\text{AgBiBr}_6/\text{Ti}_3\text{C}_2\text{T}_x$ heterostructures at different time delays after photoexcitation. Besides of the negative PB feature around 439 nm, a positive feature around 480 nm belongs to the injection of “hot carrier” and electron trapping were observed, as shown

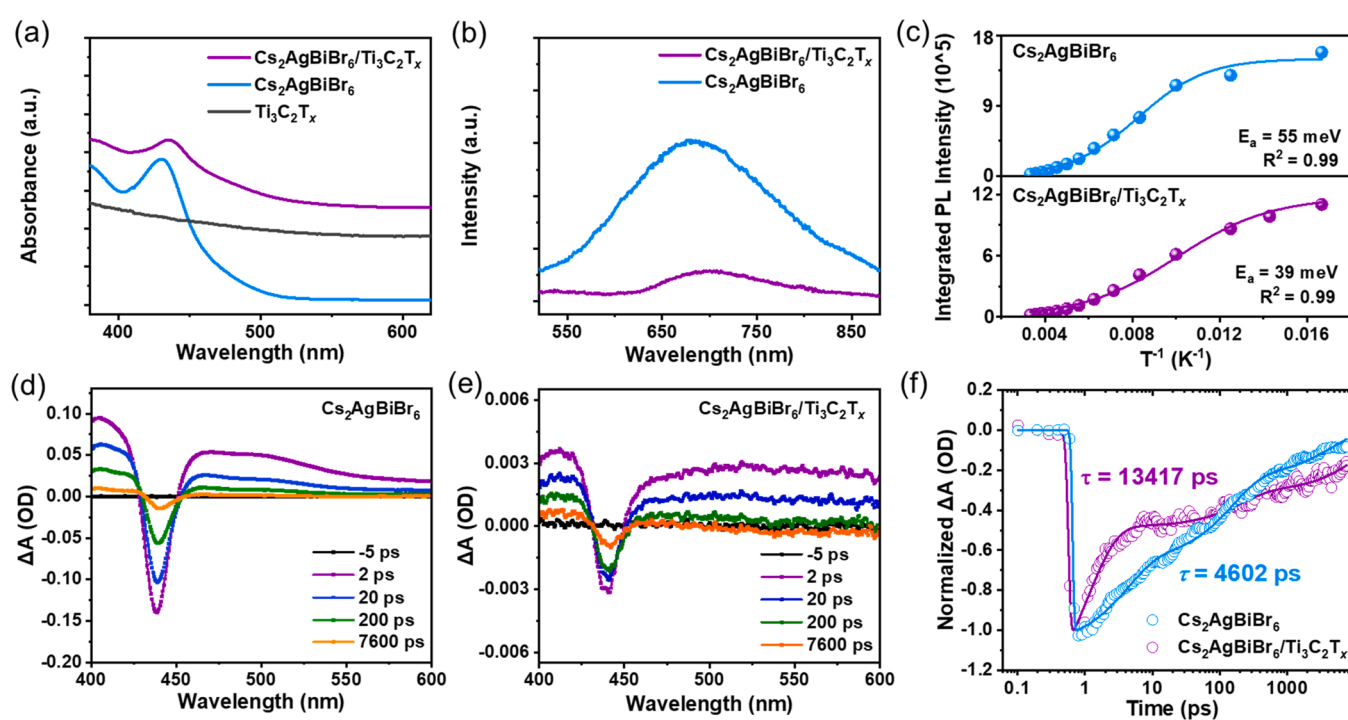


Fig. 2. (a) Optical absorption spectra of $\text{Cs}_2\text{AgBiBr}_6$ NCs, $\text{Ti}_3\text{C}_2\text{T}_x$ nanosheets and $\text{Cs}_2\text{AgBiBr}_6/\text{Ti}_3\text{C}_2\text{T}_x$ heterostructures. (b) Room-temperature PL spectra of $\text{Cs}_2\text{AgBiBr}_6$ NCs and $\text{Cs}_2\text{AgBiBr}_6/\text{Ti}_3\text{C}_2\text{T}_x$ heterostructures. (c) Integrated PL emission intensity as a function of temperature from 40 to 300 K for the extraction of exciton binding energy (up for $\text{Cs}_2\text{AgBiBr}_6$ NCs and bottom for $\text{Cs}_2\text{AgBiBr}_6/\text{Ti}_3\text{C}_2\text{T}_x$ heterostructures). Transient absorption spectra at different delay times of (d) $\text{Cs}_2\text{AgBiBr}_6$ NCs and (e) $\text{Cs}_2\text{AgBiBr}_6/\text{Ti}_3\text{C}_2\text{T}_x$ heterostructures upon photoexcitation at 370 nm. (f) The corresponding TA kinetic traces monitored at 439 nm photobleaching upon photoexcitation at 370 nm.

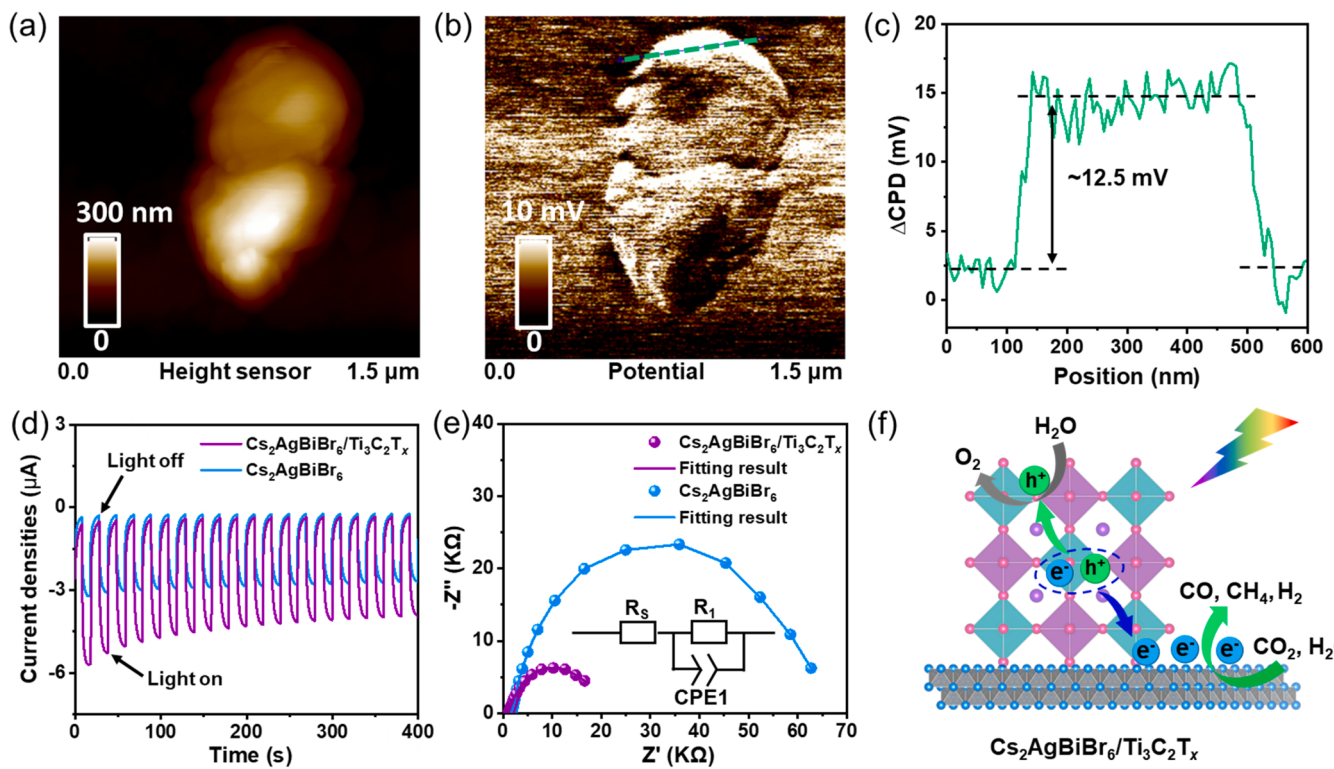


Fig. 3. (a) AFM height image and (b) surface photovoltage (SPV) image ($\Delta\text{CPD} = \text{CPD}_{\text{light}} - \text{CPD}_{\text{dark}}$) of $\text{Cs}_2\text{AgBiBr}_6/\text{Ti}_3\text{C}_2\text{T}_x$ heterostructures. (c) The corresponding line profile of SPV difference in (b). (d) The transient photocurrent response curves of $\text{Cs}_2\text{AgBiBr}_6$ and $\text{Cs}_2\text{AgBiBr}_6/\text{Ti}_3\text{C}_2\text{T}_x$ heterostructures. (e) Nyquist plots of $\text{Cs}_2\text{AgBiBr}_6$ and $\text{Cs}_2\text{AgBiBr}_6/\text{Ti}_3\text{C}_2\text{T}_x$ heterostructures under light irradiation. (f) Schematic mechanism of photocatalytic CO_2 reduction by $\text{Cs}_2\text{AgBiBr}_6/\text{Ti}_3\text{C}_2\text{T}_x$ heterostructures under visible light irradiation.

In Fig. 3c [65], Compared to $\text{Cs}_2\text{AgBiBr}_6$, the TA spectra of $\text{Cs}_2\text{AgBiBr}_6/\text{Ti}_3\text{C}_2\text{T}_x$ heterostructures show a broad and long-lived photoinduced absorption (PIA) feature in the UV-vis region, which is attributed to the excited state absorption of $\text{Ti}_3\text{C}_2\text{T}_x$ (see Fig. S13). In kinetics aspect, by following the time-profile of exciton bleaching feature at 439 nm (Fig. 2 f), there obviously demonstrates a set of changes in velocity gradient before and after the time window of several picoseconds. The fast former decay with lifetime of 1.1 ps is assigned to the ultrafast charge separation, that is, the electron transfer from $\text{Cs}_2\text{AgBiBr}_6$ to $\text{Ti}_3\text{C}_2\text{T}_x$ [66]. The electron transfer process is energy favorable according to ultraviolet photoelectron spectroscopy (UPS) analysis (Fig. S14). The latter recovery appears much more sluggish, and the fitted time-profile exhibits a long lifetime of 13417 ps, which is 1.9-fold longer than pure $\text{Cs}_2\text{AgBiBr}_6$ system (4602 ps). This indicates the existence of a long-lived charge separated state after photoexcitation in $\text{Cs}_2\text{AgBiBr}_6/\text{Ti}_3\text{C}_2\text{T}_x$ heterostructures. The fast charge transfer process and long-lived charge-separated state in $\text{Cs}_2\text{AgBiBr}_6/\text{Ti}_3\text{C}_2\text{T}_x$ heterostructures indicate the efficient charge extraction and suppressed charge recombination in $\text{Cs}_2\text{AgBiBr}_6$ NCs [67,68].

3.3. Charge separation verified by Kelvin probe force microscopy and electrochemical characterization

To further corroborate the charge separation/transfer process in $\text{Cs}_2\text{AgBiBr}_6/\text{Ti}_3\text{C}_2\text{T}_x$ heterostructures, Kelvin probe force microscopy (KPFM) was used to study the surface potential distribution. The AFM height mapping image in Fig. 3a demonstrates a typical $\text{Cs}_2\text{AgBiBr}_6/\text{Ti}_3\text{C}_2\text{T}_x$ morphology, which was selected to analyze the surface potential change before and after illumination. Under illumination, the local surface potential of $\text{Cs}_2\text{AgBiBr}_6/\text{Ti}_3\text{C}_2\text{T}_x$ heterostructures increases obviously (Fig. S15). The KPFM image and the corresponding line profiles of the SPV difference are displayed in Fig. 3b,c. A distinct positive

SPV around 12.5 mV is observed at the surface of $\text{Cs}_2\text{AgBiBr}_6/\text{Ti}_3\text{C}_2\text{T}_x$ heterostructures, indicating the accumulation of positive charges on the surface $\text{Cs}_2\text{AgBiBr}_6$ NCs [43]. In other words, the photogenerated electrons are transferred from $\text{Cs}_2\text{AgBiBr}_6$ to $\text{Ti}_3\text{C}_2\text{T}_x$, leaving holes accumulating in $\text{Cs}_2\text{AgBiBr}_6$ NCs after illumination.

The electrochemical performance associated with photogenerated charge transfer and separation was also characterized. Fig. 3d exhibits the chopped photocurrent curves of pristine $\text{Cs}_2\text{AgBiBr}_6$ and $\text{Cs}_2\text{AgBiBr}_6/\text{Ti}_3\text{C}_2\text{T}_x$ heterostructures. It can be found that $\text{Cs}_2\text{AgBiBr}_6/\text{Ti}_3\text{C}_2\text{T}_x$ heterostructures produce a photocurrent of $\sim 4.05 \mu\text{A cm}^{-2}$, approximately 60% higher than that of pristine $\text{Cs}_2\text{AgBiBr}_6$ ($\sim 2.56 \mu\text{A cm}^{-2}$), implying that the photoexcited charge carrier separation in $\text{Cs}_2\text{AgBiBr}_6/\text{Ti}_3\text{C}_2\text{T}_x$ heterostructures is largely promoted [69–72]. The increased photocurrent density verified the quenched PL emission of $\text{Cs}_2\text{AgBiBr}_6$ after hybridization with $\text{Ti}_3\text{C}_2\text{T}_x$ is attributed to the facilitated charge separation rather than trap-assisted nonradiative recombination. To further examine the impact of $\text{Ti}_3\text{C}_2\text{T}_x$ on the charge transfer properties of $\text{Cs}_2\text{AgBiBr}_6$, the electrochemical impedance spectroscopy (EIS) plots were measured. As shown in Fig. 3e, the Nyquist plots indicate that the charge transfer resistance obviously decreased for the $\text{Cs}_2\text{AgBiBr}_6/\text{Ti}_3\text{C}_2\text{T}_x$ film, as evidenced by the smaller semicircle arc at high frequencies and the corresponding fitting results (62,316 ohms for $\text{Cs}_2\text{AgBiBr}_6$ NCs and 18,440 ohms for $\text{Cs}_2\text{AgBiBr}_6/\text{Ti}_3\text{C}_2\text{T}_x$) [73–75]. Based on the above discussion, the photogenerated electrons in the $\text{Cs}_2\text{AgBiBr}_6$ can be effectively transferred to MXene nanosheets and get separated from photogenerated holes, leading to a long-lived charge-separated state (Fig. 3f), which may largely improve the photocatalytic performance of $\text{Cs}_2\text{AgBiBr}_6/\text{Ti}_3\text{C}_2\text{T}_x$ heterostructures. These photogenerated electrons in MXene can effectively react with adsorbed CO_2 and H_2O molecules to produce CO , CH_4 and H_2 [11,12]. On the other hand, the photogenerated holes are quenched by H_2O molecules to generate O_2 , as evidenced by the GC spectrum of the CO_2 reduction

products in Fig. S16, which is similar to previous reports [12,76].

3.4. Photocatalytic CO₂ reduction performance of Cs₂AgBiBr₆/Ti₃C₂T_x heterostructures

As a proof-of-concept application, we applied the Cs₂AgBiBr₆/Ti₃C₂T_x heterostructures as photocatalysts in CO₂ reduction. Fig. 4a shows the amounts of H₂, CO and CH₄ produced after 1 h of photocatalytic CO₂ reduction for Cs₂AgBiBr₆ NCs, Cs₂AgBiBr₆/Ti₃C₂T_x heterostructures, and Ti₃C₂T_x nanosheets, respectively. As expected, Cs₂AgBiBr₆/Ti₃C₂T_x heterostructures exhibit superior catalytic performance than pristine Cs₂AgBiBr₆ NCs and Ti₃C₂T_x nanosheets. Specifically, the total product yield of the Cs₂AgBiBr₆/Ti₃C₂T_x heterostructures is 21.4 μmol g⁻¹ (8.9 μmol g⁻¹ for H₂, 11.1 μmol g⁻¹ for CO, and 1.3 μmol g⁻¹ for CH₄), which is much higher than that of pristine Cs₂AgBiBr₆ NCs (12.4 μmol g⁻¹) and Ti₃C₂T_x nanosheets (5.5 μmol g⁻¹) (Table S3). The outputs of all products grow almost linearly with prolonging the reaction time (Fig. 4b and S17). The product selectivity for CO of Cs₂AgBiBr₆ is calculated to be 70.9% (Table S3). Compared to Cs₂AgBiBr₆, the selectivity of Cs₂AgBiBr₆/Ti₃C₂T_x heterostructures for CO is decreased to 52.1% due to the higher H₂O adsorption capacity of Ti₃C₂T_x [77]. When irradiated by visible light, the photogenerated electrons in the conduction band (CB) of Cs₂AgBiBr₆ could be extracted rapidly by the Ti₃C₂T_x nanosheets. These photo-generated electrons in Ti₃C₂T_x nanosheets then largely produce H₂ and CH₄ by consuming the water molecules. As such, the selectivity of Cs₂AgBiBr₆/Ti₃C₂T_x heterostructures for H₂ and CH₄ is enhanced compared to bare Cs₂AgBiBr₆, which is consistent with the photo-generated electron transfer from Cs₂AgBiBr₆ to Ti₃C₂T_x. In the aspect of effective photoelectrons participated in the reaction, the electron consumption yield of Cs₂AgBiBr₆/Ti₃C₂T_x heterostructures is calculated to be 50.6 μmol g⁻¹ h⁻¹, which is about 98.4% and 148.0% increment compared to pristine Cs₂AgBiBr₆ NCs (25.5 μmol g⁻¹ h⁻¹) and Ti₃C₂T_x nanosheets (20.4 μmol g⁻¹ h⁻¹), as shown in Fig. 4c. The electron

consumption yield (50.6 μmol g⁻¹ h⁻¹) obtained here for Cs₂AgBiBr₆/Ti₃C₂T_x heterostructures is higher than most previously reported lead-free perovskite-based catalysts (Table S4). The AQY of Cs₂AgBiBr₆/MXene during the 5 h reaction time was calculated to be 0.083%, 0.071%, and 0.005% at 485, 535 and 595 nm, respectively, which is consistent with the light absorption of the material. Based on the above analyses, the remarkable photocatalytic performance of Cs₂AgBiBr₆/Ti₃C₂T_x heterostructures can be mainly attributed to the efficient photogenerated charge separation and transport as well as the improved surface area and CO₂ adsorption ability. Additionally, no obvious decomposition and morphology change of Cs₂AgBiBr₆/Ti₃C₂T_x heterostructures were found during the photocatalytic reaction process (Fig. S18 and S19).

To identify the source of CO₂ photoreduction products, isotopically ¹³CO₂ gas was used as the source, and the products were detected by gas chromatography/mass spectrometry (GC/MS). As shown in Fig. S20, signals with the mass-to-charge ratio (*m/z*) values of 29 and 45 (ascribed to ¹³CO and ¹³CO₂) can be detected, demonstrating the fact that the reductive products are generated from the photocatalytic CO₂ reduction reaction. It should be noted that the signal of ¹³CH₄ was too weak to be detected due to the low yield. The possible reaction intermediate and pathway calculated by the spin-polarized density functional theories (DFT) in Fig. S21 also suggest CO₂ are prone to be reduced as CO and CH₄ simultaneously [78].

The recycling photocatalytic cycle tests of Cs₂AgBiBr₆/Ti₃C₂T_x heterostructures were performed to investigate the catalytic stability. As shown in Fig. 4d, the electron consumption yield remains almost unchanged after cycling 3 times. No obvious decomposition and morphology change of Cs₂AgBiBr₆/Ti₃C₂T_x can be observed from the corresponding XRD patterns and TEM image in Fig. S22, indicating the good stability of the heterostructures.

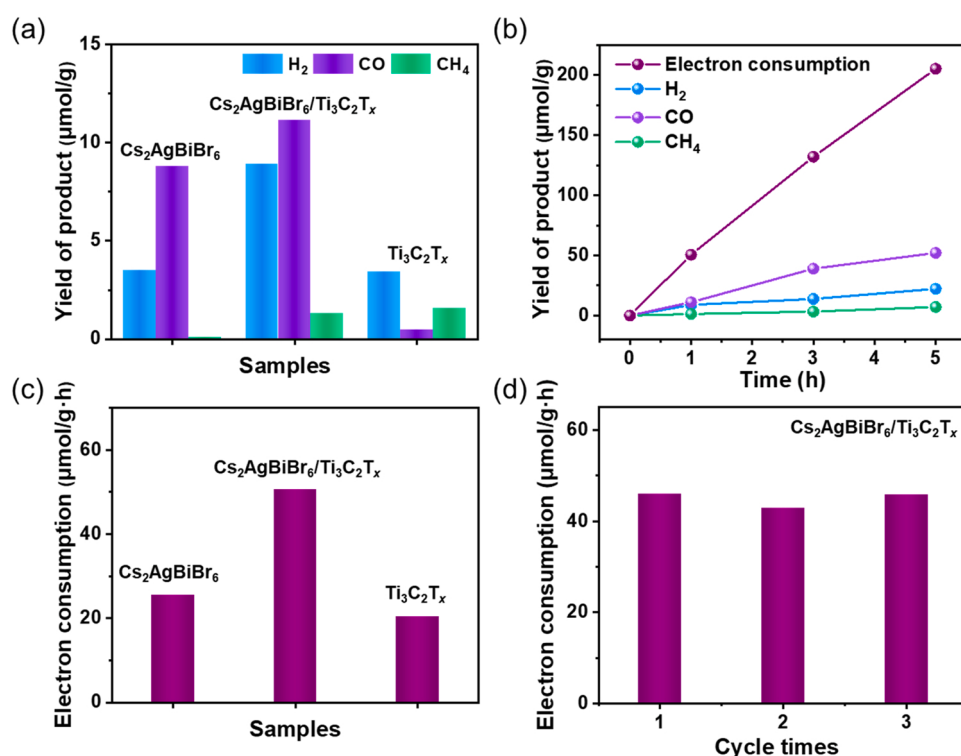


Fig. 4. (a) Comparison of the photocatalytic activity of Cs₂AgBiBr₆, Ti₃C₂T_x and Cs₂AgBiBr₆/Ti₃C₂T_x heterostructures for CO₂ reduction. (b) Long-term photocatalytic tests of Cs₂AgBiBr₆/Ti₃C₂T_x heterostructures. (c) The average electron consumption of different samples after 1 h of photochemical reaction for CO₂ reduction. (d) Recycling tests of Cs₂AgBiBr₆/Ti₃C₂T_x heterostructures for 3 times.

4. Conclusions

In conclusion, lead-free double perovskite $\text{Cs}_2\text{AgBiBr}_6$ NCs were self-assembled on few-layer MXene nanosheets via mutual Coulomb electrostatic interaction for the first time. The presence of MXene nanosheets effectively reduces exciton binding energy of $\text{Cs}_2\text{AgBiBr}_6$ NCs and simultaneously promotes the efficient formation of free charge carriers. The ultrafast photogenerated electron transfer from $\text{Cs}_2\text{AgBiBr}_6$ to MXene with a timescale of 1.1 ps largely prolongs the charge carrier lifetime by two times due to suppressed carrier recombination. As a result of the efficient charge separation and electron extraction as well as an improved surface area and CO_2 adsorption ability, the $\text{Cs}_2\text{AgBiBr}_6$ /MXene heterostructures achieve a high photoelectron consumption yield of $50.6 \mu\text{mol g}^{-1} \text{h}^{-1}$ for photocatalytic CO_2 reduction. This work may provide a useful guidance for the use of lead-free halide perovskite/2D material heterostructures in photocatalysis and various other photovoltaic applications.

CRediT authorship contribution statement

Zhipeng Zhang: Investigation, Writing – original draft preparation. **Bingzhe Wang:** Investigation. **Hai-Bing Zhao:** Investigation. **Jin-Feng Liao:** Investigation. **Zi-Chun Zhou:** Investigation. **Tanghao Liu:** Investigation. **Bingchen He:** Investigation. **Qi Wei:** Investigation. **Shi Chen:** Investigation. **Hong-Yan Chen:** Investigation. **Dai-Bin Kuang:** Writing – review & editing, Supervision. **Ying Li:** Writing – review & editing, Supervision. **Guichuan Xing:** Supervision, Funding acquisition.

Declaration of Competing Interest

The authors declare that they have no known competing financial interests or personal relationships that could have appeared to influence the work reported in this paper.

Acknowledgements

The authors acknowledge the Science and Technology Development Fund, Macao SAR (File no. FDCT-0044/2020/A1, FDCT-014/2017/AMJ), UM's Research Fund (File no. MYRG2018-00148-IAPME, MYRG2020-00151-IAPME), the Natural Science Foundation of China (61935017, 61904152, 21875288), Natural Science Foundation of Guangdong Province, China (2019A1515012186), Guangdong-Hong Kong-Macao Joint Laboratory of Optoelectronic and Magnetic Functional Materials (2019B121205002), and Shenzhen-Hong Kong-Macao Science and Technology Innovation Project (Category C) (SGDX2020110309360100). Special thanks to Dr. Yang-Fan Xu for the valuable discussion on the catalytic mechanism.

Appendix A. Supporting information

Supplementary data associated with this article can be found in the online version at [doi:10.1016/j.apcatb.2022.121358](https://doi.org/10.1016/j.apcatb.2022.121358).

References

- [1] Y. Wei, Z. Cheng, J. Lin, An overview on enhancing the stability of lead halide perovskite quantum dots and their applications in phosphor-converted LEDs, *Chem. Soc. Rev.* 48 (2019) 310–350.
- [2] Y. Yuan, H. Zhu, K. Hills-Kimball, T. Cai, W. Shi, Z. Wei, H. Yang, Y. Candler, P. Wang, J. He, O. Chen, Stereoselective C-C oxidative coupling reactions photocatalyzed by zwitterionic ligand capped CsPbBr_3 perovskite quantum dots, *Angew. Chem. Int. Ed.* 59 (2020) 22563–22569.
- [3] L. Duan, L. Hu, X. Guan, C.-H. Lin, D. Chu, S. Huang, X. Liu, J. Yuan, T. Wu, Quantum dots for photovoltaics: a tale of two materials, *Adv. Energy Mater.* 11 (2021), 2100354.
- [4] Y.-H. Kim, S. Kim, A. Kakekhani, J. Park, J. Park, Y.-H. Lee, H. Xu, S. Nagane, R. B. Wexler, D.-H. Kim, S.H. Jo, L. Martínez-Sarti, P. Tan, A. Sadhanala, G.-S. Park, Y.-W. Kim, B. Hu, H.J. Bolink, S. Yoo, R.H. Friend, A.M. Rappe, T.-W. Lee, Comprehensive defect suppression in perovskite nanocrystals for high-efficiency light-emitting diodes, *Nat. Photon.* 15 (2021) 148–155.
- [5] M.V. Kovalenko, L. Protesescu, M.I. Bodnarchuk, Properties and potential optoelectronic applications of lead halide perovskite nanocrystals, *Science* 358 (2017) 745–750.
- [6] M. Liu, Q. Wan, H. Wang, F. Carulli, X. Sun, W. Zheng, L. Kong, Q. Zhang, C. Zhang, Q. Zhang, S. Brovelli, L. Li, Suppression of temperature quenching in perovskite nanocrystals for efficient and thermally stable light-emitting diodes, *Nat. Photon.* 15 (2021) 379–385.
- [7] C.-H. Lu, G.V. Biesold-McGee, Y. Liu, Z. Kang, Z. Lin, Doping and ion substitution in colloidal metal halide perovskite nanocrystals, *Chem. Soc. Rev.* 49 (2020) 4953–5007.
- [8] Y. Jiang, J.-F. Liao, H.-Y. Chen, H.-H. Zhang, J.-Y. Li, X.-D. Wang, D.-B. Kuang, All-solid-state Z-scheme $\alpha\text{-Fe}_2\text{O}_3$ /amine-RGO/ CsPbBr_3 hybrids for visible-light-driven photocatalytic CO_2 reduction, *Chem* 6 (2020) 766–780.
- [9] M. Ou, W. Tu, S. Yin, W. Xing, S. Wu, H. Wang, S. Wan, Q. Zhong, R. Xu, Amino-assisted anchoring of CsPbBr_3 perovskite quantum dots on porous g-C₃N₄ for enhanced photocatalytic CO_2 reduction, *Angew. Chem. Int. Ed.* 57 (2018) 13570–13574.
- [10] A. Kumar, A. Kumar, V. Krishnan, Perovskite oxide based materials for energy and environment-oriented photocatalysis, *ACS Catal.* 10 (2020) 10253–10315.
- [11] X. Wang, J. He, J. Li, G. Lu, F. Dong, T. Majima, M. Zhu, Immobilizing perovskite CsPbBr_3 nanocrystals on black phosphorus nanosheets for boosting charge separation and photocatalytic CO_2 reduction, *Appl. Catal. B Environ.* 277 (2020), 119230.
- [12] X. Wang, J. He, L. Mao, X. Cai, C. Sun, M. Zhu, CsPbBr_3 perovskite nanocrystals anchoring on monolayer MoS₂ nanosheets for efficient photocatalytic CO_2 reduction, *Chem. Eng. J.* 416 (2021), 128077.
- [13] X.D. Wang, Y.H. Huang, J.F. Liao, Y. Jiang, L. Zhou, X.Y. Zhang, H.Y. Chen, D. B. Kuang, In situ construction of a Cs_2SnI_6 perovskite nanocrystal/SnS₂ nanosheet heterojunction with boosted interfacial charge transfer, *J. Am. Chem. Soc.* 141 (2019) 13434–13441.
- [14] Z. Zhang, S. Wang, X. Liu, Y. Chen, C. Su, Z. Tang, Y. Li, G. Xing, Metal halide perovskite/2D material heterostructures: syntheses and applications, *Small Methods* 5 (2021), 2000937.
- [15] X. Meng, Y. Wang, J. Lin, X. Liu, X. He, J. Barbaud, T. Wu, T. Noda, X. Yang, L. Han, Surface-controlled oriented growth of FASnI₃ crystals for efficient lead-free perovskite solar cells, *Joule* 4 (2020) 902–912.
- [16] Z. Tan, Y. Chu, J. Chen, J. Li, G. Ji, G. Niu, L. Gao, Z. Xiao, J. Tang, Lead-free perovskite variant solid solutions $\text{Cs}_2\text{Sn}_{1-x}\text{Te}_x\text{Cl}_x$: bright luminescence and high anti-water stability, *Adv. Mater.* 32 (2020), 2002443.
- [17] T.C. Jellicoe, J.M. Richter, H.F.J. Glass, M. Tabachnyk, R. Brady, S.E. Dutton, A. Rao, R.H. Friend, D. Credgington, N.C. Greenham, M.L. Böhm, Synthesis and optical properties of lead-free cesium tin halide perovskite nanocrystals, *J. Am. Chem. Soc.* 138 (2016) 2941–2944.
- [18] B. Yang, J. Chen, F. Hong, X. Mao, K. Zheng, S. Yang, Y. Li, T. Pullerits, W. Deng, K. Han, Lead-free, air-stable all-inorganic cesium bismuth halide perovskite nanocrystals, *Angew. Chem. Int. Ed.* 56 (2017) 12471–12475.
- [19] Q. Wei, M. Li, Z. Zhang, J. Guo, G. Xing, T.C. Sum, W. Huang, Efficient recycling of trapped energies for dual-emission in Mn-doped perovskite nanocrystals, *Nano Energy* 51 (2018) 704–710.
- [20] Q. Fan, G.V. Biesold-McGee, J. Ma, Q. Xu, S. Pan, J. Peng, Z. Lin, Lead-free halide perovskite nanocrystals: crystal structures, synthesis, stabilities, and optical properties, *Angew. Chem. Int. Ed.* 59 (2020) 1030–1046.
- [21] C. Kang, H. Rao, Y. Fang, J. Zeng, Z. Pan, X. Zhong, Antioxidative stannous oxalate derived lead-free stable CsSnX₃ (X=Cl, Br, and I) perovskite nanocrystals, *Angew. Chem. Int. Ed.* 60 (2021) 660–665.
- [22] Z. Zhang, Y. Liang, H. Huang, X. Liu, Q. Li, L. Chen, D. Xu, Stable and highly efficient photocatalysis with lead-free double-perovskite of $\text{Cs}_2\text{AgBiBr}_6$, *Angew. Chem. Int. Ed.* 58 (2019) 7263–7267.
- [23] Y. Bekenstein, J.C. Dahl, J. Huang, W.T. Osowiecki, J.K. Swabek, E.M. Chan, P. Yang, A.P. Alivisatos, The making and breaking of lead-free double perovskite nanocrystals of cesium silver-bismuth halide compositions, *Nano Lett.* 18 (2018) 3502–3508.
- [24] C. Wu, Q. Zhang, Y. Liu, W. Luo, X. Guo, Z. Huang, H. Ting, W. Sun, X. Zhong, S. Wei, S. Wang, Z. Chen, L. Xiao, The dawn of lead-free perovskite solar cell: highly stable double perovskite $\text{Cs}_2\text{AgBiBr}_6$ film, *Adv. Sci.* 5 (2018), 1700759.
- [25] D. Wu, X. Zhao, Y. Huang, J. Lai, H. Li, J. Yang, C. Tian, P. He, Q. Huang, X. Tang, Lead-free perovskite $\text{Cs}_2\text{AgBiX}_6$ nanocrystals with a band gap funnel structure for photocatalytic CO_2 reduction under visible light, *Chem. Mater.* 33 (2021) 4971–4976.
- [26] S. Kumar, I. Hassan, M. Regue, S. Gonzalez-Carrero, E. Rattner, M.A. Isaacs, S. Eslava, Mechanochemically synthesized Pb-free halide perovskite-based $\text{Cs}_2\text{AgBiBr}_6\text{-Cu-RGO}$ nanocomposite for photocatalytic CO_2 reduction, *J. Mater. Chem. A* 9 (2021) 12179–12187.
- [27] L. Zhou, Y.F. Xu, B.X. Chen, D.B. Kuang, C.Y. Su, Synthesis and photocatalytic application of stable lead-free $\text{Cs}_2\text{AgBiBr}_6$ perovskite nanocrystals, *Small* 14 (2018), 1703762.
- [28] T. Wang, D. Yue, X. Li, Y. Zhao, Lead-free double perovskite $\text{Cs}_2\text{AgBiBr}_6/\text{RGO}$ composite for efficient visible light photocatalytic H_2 evolution, *Appl. Catal. B Environ.* 268 (2019), 118399.
- [29] Y. Wang, H. Huang, Z. Zhang, C. Wang, Y. Yang, Q. Li, D. Xu, Lead-free perovskite $\text{Cs}_2\text{AgBiBr}_6@g\text{-C}_3\text{N}_4$ Z-scheme system for improving CH_4 production in photocatalytic CO_2 reduction, *Appl. Catal. B Environ.* 282 (2021), 119570.
- [30] A. Dey, A.F. Richter, T. Debnath, H. Huang, L. Polavarapu, J. Feldmann, A.C. S. Nano, Transfer of direct to indirect bound excitons by electron intervalley

scattering in $\text{Cs}_2\text{AgBiBr}_6$ double perovskite nanocrystals, *ACS nano* 14 (2020) 5855–5861.

[31] T. Li, X. Zhao, D. Yang, M.-H. Du, L. Zhang, Intrinsic defect properties in halide double perovskites for optoelectronic applications, *Phys. Rev. Appl.* 10 (2018), 041001.

[32] Z. Liu, H. Yang, J. Wang, Y. Yuan, K. Hills-Kimball, T. Cai, P. Wang, A. Tang, O. Chen, Synthesis of lead-free $\text{Cs}_2\text{AgBiX}_6$ ($X = \text{Cl}, \text{Br}, \text{I}$) double perovskite nanoplatelets and their application in CO_2 photocatalytic reduction, *Nano Lett.* 21 (2021) 1620–1627.

[33] J.L. Hart, K. Hantanasisirakul, A.C. Lang, B. Anasori, D. Pinto, Y. Pivak, J.T. van Omme, S.J. May, Y. Gogotsi, M.L. Taheri, Control of MXenes' electronic properties through termination and intercalation, *Nat. Commun.* 10 (2019) 522.

[34] J. Pang, R.G. Mendes, A. Bachmatiuk, L. Zhao, H.Q. Ta, T. Gemming, H. Liu, Z. Liu, M.H. Rummeli, Applications of 2D MXenes in energy conversion and storage systems, *Chem. Soc. Rev.* 48 (2019) 72–133.

[35] B. Anasori, M.R. Lukatskaya, Y. Gogotsi, 2D metal carbides and nitrides (MXenes) for energy storage, *Nat. Rev. Mater.* 2 (2017) 16098.

[36] L. Zhao, B. Dong, S. Li, L. Zhou, L. Lai, Z. Wang, S. Zhao, M. Han, K. Gao, M. Lu, X. Xie, B. Chen, Z. Liu, X. Wang, H. Zhang, H. Li, J. Liu, H. Zhang, X. Huang, W. Huang, Interdiffusion reaction-assisted hybridization of two-dimensional metal-organic frameworks and $\text{Ti}_3\text{C}_2\text{T}_x$ nanosheets for electrocatalytic oxygen evolution, *ACS Nano* 11 (2017) 5800–5807.

[37] F. Ming, H. Liang, W. Zhang, J. Ming, Y. Lei, A.-H. Emwas, H.N. Alshareef, Porous MXenes enable high performance potassium ion capacitors, *Nano Energy* 62 (2019) 853–860.

[38] C. Tang, Y. Min, C. Chen, W. Xu, L. Xu, Potential applications of heterostructures of TMDs with MXenes in sodium-ion and Na-O_2 batteries, *Nano Lett.* 19 (2019) 5577–5586.

[39] B. Lyu, M. Kim, H. Jing, J. Kang, C. Qian, S. Lee, J.H. Cho, Large-area MXene electrode array for flexible electronics, *ACS Nano* 13 (2019) 11392–11400.

[40] J. Liu, H.-B. Zhang, R. Sun, Y. Liu, Z. Liu, A. Zhou, Z.-Z. Yu, Hydrophobic, flexible, and lightweight MXene foams for high-performance electromagnetic-interference shielding, *Adv. Mater.* 29 (2017), 1702367.

[41] G. Eda, S.A. Maier, Two-dimensional crystals: managing light for optoelectronics, *ACS Nano* 7 (2013) 5660–5665.

[42] Z. Zhang, F. Sun, Z. Zhu, J. Dai, K. Gao, Q. Wei, X. Shi, Q. Sun, Y. Yan, H. Li, H. Yu, G. Xing, X. Huang, W. Huang, Unconventional solution-phase epitaxial growth of organic-inorganic hybrid perovskite nanocrystals on metal sulfide nanosheets, *Sci. China Mater.* 62 (2019) 43–53.

[43] Y. Jiang, H.-Y. Chen, J.-Y. Li, J.-F. Liao, H.-H. Zhang, X.-D. Wang, D.-B. Kuang, Z-Scheme 2D/2D heterojunction of $\text{CsPbBr}_3/\text{Bi}_2\text{WO}_6$ for improved photocatalytic CO_2 reduction, *Adv. Funct. Mater.* 30 (2020), 2004293.

[44] Y. Zhao, S. Zhang, R. Shi, G.I.N. Waterhouse, J. Tang, T. Zhang, Two-dimensional photocatalyst design: a critical review of recent experimental and computational advances, *Mater. Today* 34 (2020) 78–91.

[45] F. Han, S. Luo, L. Xie, J. Zhu, W. Wei, X. Chen, F. Liu, W. Chen, J. Zhao, L. Dong, K. Yu, X. Zeng, F. Rao, L. Wang, Y. Huang, Boosting the yield of MXene 2D sheets via a facile hydrothermal-assisted intercalation, *ACS Appl. Mater. Interfaces* 11 (2019) 8443–8452.

[46] Y. Liu, H. Xiao, W.A. Goddard, Schottky-barrier-free contacts with two-dimensional semiconductors by surface-engineered MXenes, *J. Am. Chem. Soc.* 138 (2016) 15853–15856.

[47] Z. Zhang, Y. Li, C. Liang, G. Yu, J. Zhao, S. Luo, Y. Huang, C. Su, G. Xing, In situ growth of MAPbBr_3 nanocrystals on few-layer MXene nanosheets with efficient energy transfer, *Small* 16 (2020), 1905896.

[48] A. Pan, X. Ma, S. Huang, Y. Wu, M. Jia, P. Wangyang, Y. Liu, Y. Shi, L. He, Y. Liu, CsPbBr_3 perovskite nanocrystal grown on MXene nanosheets for enhanced photoelectric detection and photocatalytic CO_2 reduction, *J. Phys. Chem. Lett.* 10 (2019) 6590–6597.

[49] X. Luo, G. Liang, J. Wang, X. Liu, K. Wu, Picosecond multi-hole transfer and microsecond charge-separated states at the perovskite nanocrystal/tetracene interface, *Chem. Sci.* 10 (2019) 2459–2464.

[50] Z. Chen, Y. Hu, J. Wang, Q. Shen, Y. Zhang, C. Ding, Y. Bai, G. Jiang, Z. Li, N. Gaponik, Boosting photocatalytic CO_2 reduction on CsPbBr_3 perovskite nanocrystals by immobilizing metal complexes, *Chem. Mater.* 32 (2020) 1517–1525.

[51] O. Mashtalar, M. Naguib, V.N. Mochalin, Y. Dall'Agneze, M. Heon, M.W. Barsoum, Y. Gogotsi, Intercalation and delamination of layered carbides and carbonitrides, *Nat. Commun.* 4 (2013) 1716.

[52] Z. Wang, Z. Xu, H. Huang, X. Chu, Y. Xie, D. Xiong, C. Yan, H. Zhao, H. Zhang, W. Yang, Unraveling and regulating self-discharge behavior of $\text{Ti}_3\text{C}_2\text{T}_x$ MXene-based supercapacitors, *ACS Nano* 14 (2020) 4916–4924.

[53] J.-F. Liao, Y.-F. Xu, X.-D. Wang, H.-Y. Chen, D.-B. Kuang, CsPbBr_3 nanocrystal/ MO_2 ($\text{M} = \text{Si}, \text{Ti}, \text{Sn}$) composites: insight into charge-carrier dynamics and photoelectrochemical applications, *ACS Appl. Mater. Interfaces* 10 (2018) 42301–42309.

[54] K. Chen, X. Deng, G. Dodekatos, H. Tüysüz, Photocatalytic polymerization of 3,4-ethylenedioxythiophene over cesium lead iodide perovskite quantum dots, *J. Am. Chem. Soc.* 139 (2017) 12267–12273.

[55] B. Tang, Z.G. Yu, H.L. Seng, N. Zhang, X. Liu, Y.-W. Zhang, W. Yang, H. Gong, Simultaneous edge and electronic control of MoS_2 nanosheets through Fe doping for an efficient oxygen evolution reaction, *Nanoscale* 10 (2018) 20113–20119.

[56] J. Lin, P. Wang, H. Wang, C. Li, X. Si, J. Qi, J. Cao, Z. Zhong, W. Fei, J. Feng, Defect-rich heterogeneous $\text{MoS}_2/\text{NiS}_2$ nanosheets electrocatalysts for efficient overall water splitting, *Adv. Sci.* 6 (2019), 1900246.

[57] L. An, J. Feng, Y. Zhang, R. Wang, H. Liu, G.-C. Wang, F. Cheng, P. Xi, Epitaxial heterogeneous interfaces on $\text{NiMoO}_4/\text{NiS}_2$ nanowires/nanosheets to boost hydrogen and oxygen production for overall water splitting, *Adv. Funct. Mater.* 29 (2019), 1805298.

[58] Y. Lee, J. Kwon, E. Hwang, C.H. Ra, W.J. Yoo, J.H. Ahn, J.H. Park, J.H. Cho, High-performance perovskite-graphene hybrid photodetector, *Adv. Mater.* 27 (2015) 41–46.

[59] C. Ma, Y.M. Shi, W.J. Hu, M.H. Chiu, Z.X. Liu, A. Bera, F. Li, H. Wang, L.J. Li, T. Wu, Heterostructured $\text{WS}_2/\text{CH}_3\text{NH}_3\text{PbI}_3$ photoconductors with suppressed dark current and enhanced photodetectivity, *Adv. Mater.* 28 (2016) 3683–3689.

[60] M. Leng, Y. Yang, Z. Chen, W. Gao, J. Zhang, G. Niu, D. Li, H. Song, J. Zhang, S. Jin, J. Tang, Surface passivation of bismuth-based perovskite variant quantum dots to achieve efficient blue emission, *Nano Lett.* 18 (2018) 6076–6083.

[61] X. Li, Y. Wu, S. Zhang, B. Cai, Y. Gu, J. Song, H. Zeng, CsPbX_3 quantum dots for lighting and displays: room-temperature synthesis, photoluminescence superiorities, underlying origins and white light-emitting diodes, *Adv. Funct. Mater.* 26 (2016) 2435–2445.

[62] M.C. Gélvez-Rueda, M.B. Fridriksson, R.K. Dubey, W.F. Jager, W. van der Stam, F. C. Grozema, Overcoming the exciton binding energy in two-dimensional perovskite nanoplatelets by attachment of conjugated organic chromophores, *Nat. Commun.* 11 (2020) 1901.

[63] J. Cho, J.T. DuBose, P.V. Kamat, Charge injection from excited $\text{Cs}_2\text{AgBiBr}_6$ quantum dots into semiconductor oxides, *Chem. Mater.* 32 (2020) 510–517.

[64] E.T. McClure, M.R. Ball, W. Windl, P.M. Woodward, $\text{Cs}_2\text{AgBiX}_6$ ($X = \text{Br}, \text{Cl}$): new visible light absorbing, lead-free halide perovskite semiconductors, *Chem. Mater.* 28 (2016) 1348–1354.

[65] B. Yang, J. Chen, S. Yang, F. Hong, L. Sun, P. Han, T. Pullerits, W. Deng, K. Han, Lead-free silver-bismuth halide double perovskite nanocrystals, *Angew. Chem. Int. Ed.* 57 (2018) 5359–5363.

[66] B. Peng, G. Yu, Y. Zhao, Q. Xu, G. Xing, X. Liu, D. Fu, B. Liu, J.R. Tan, W. Tang, H. Lu, J. Xie, L. Deng, T.C. Sum, K.P. Loh, Achieving ultrafast hole transfer at the monolayer MoS_2 and $\text{CH}_3\text{NH}_3\text{PbI}_3$ perovskite interface by defect engineering, *ACS Nano* 10 (2016) 6383–6393.

[67] K. Wu, H. Zhu, Z. Liu, W. Rodriguez-Cordoba, T. Lian, Ultrafast charge separation and long-lived charge separated state in photocatalytic CdS-Pt nanorod heterostructures, *J. Am. Chem. Soc.* 134 (2012) 10337–10340.

[68] A.J. Cowan, J.R. Durrant, Long-lived charge separated states in nanostructured semiconductor photoelectrodes for the production of solar fuels, *Chem. Soc. Rev.* 42 (2013) 2281–2293.

[69] L. Huang, B. Li, B. Su, Z. Xiong, C. Zhang, Y. Hou, Z. Ding, S. Wang, Fabrication of hierarchical $\text{Co}_3\text{O}_4@\text{CdIn}_2\text{S}_4$ p-n heterojunction photocatalysts for improved CO_2 reduction with visible light, *J. Mater. Chem. A* 8 (2020) 7177–7183.

[70] R. Wang, P. Yang, S. Wang, X. Wang, Distorted carbon nitride nanosheets with activated $n \rightarrow \pi^*$ transition and preferred textural properties for photocatalytic CO_2 reduction, *J. Catal.* 402 (2021) 166–176.

[71] B. Li, W. Wang, J. Zhao, Z. Wang, B. Su, Y. Hou, Z. Ding, W.-J. Ong, S. Wang, All-solid-state direct Z-scheme $\text{NiTiO}_3/\text{Cd}_{0.5}\text{Zn}_{0.5}\text{S}$ heterostructures for photocatalytic hydrogen evolution with visible light, *J. Mater. Chem. A* 9 (2021) 10270–10276.

[72] S. Wang, B.Y. Guan, X.W.D. Lou, Construction of $\text{ZnIn}_2\text{S}_4-\text{In}_2\text{O}_3$ hierarchical tubular heterostructures for efficient CO_2 photoreduction, *J. Am. Chem. Soc.* 140 (2018) 5037–5040.

[73] Y. Wu, P. Wang, X. Zhu, Q. Zhang, Z. Wang, Y. Liu, G. Zou, Y. Dai, M.H. Whangbo, B. Huang, Composite of $\text{CH}_3\text{NH}_3\text{PbI}_3$ with reduced graphene oxide as a highly efficient and stable visible-light photocatalyst for hydrogen evolution in aqueous HI solution, *Adv. Mater.* 30 (2018), 1704342.

[74] R. Li, X. Li, J. Wu, X. Lv, Y.-Z. Zheng, Z. Zhao, X. Ding, X. Tao, J.-F. Chen, Few-layer black phosphorus-on- MAPbI_3 for superb visible-light photocatalytic hydrogen evolution from HI splitting, *Appl. Catal. B Environ.* 259 (2019), 118075.

[75] S. Wang, X. Wang, Photocatalytic CO_2 reduction by CdS promoted with a zeolitic imidazolate framework, *Appl. Catal. B Environ.* 162 (2015) 494–500.

[76] Z.-C. Kong, J.-F. Liao, Y.-J. Dong, Y.-F. Xu, H.-Y. Chen, D.-B. Kuang, C.-Y. Su, Core@Shell $\text{CsPbBr}_3@\text{Zeolitic imidazolate framework nanocomposite}$ for efficient photocatalytic CO_2 reduction, *ACS Energy Lett.* 3 (2018) 2656–2662.

[77] L. Xiu, W. Pei, S. Zhou, Z. Wang, P. Yang, J. Zhao, J. Qiu, Multilevel hollow MXene tailored low-Pt catalyst for efficient hydrogen evolution in full-pH range and seawater, *Adv. Funct. Mater.* 30 (2020), 1910028.

[78] J. Sheng, Y. He, M. Huang, C. Yuan, S. Wang, F. Dong, Frustrated lewis pair sites boosting CO_2 photoreduction on Cs_2CuBr_4 perovskite quantum dots, *ACS Catal.* 12 (2022) 2915–2926.